Landslides (2017) 14:1431–1440
DOI 10.1007/s10346-017-0795-x
Received: 21 July 2016
Accepted: 2 January 2017
Published online: 19 January 2017

Mariusz Frukacz · Andreas Wieser

On the impact of rockfall catch fences on ground-based radar interferometry

Abstract Rockfalls are major natural hazards in mountainous regions and as such monitored if they pose a high risk to people or infrastructure. Ground-based radar interferometry is a relatively new technique suitable for such monitoring. It offers the potential for determining sub-mm- to mm-level displacements by remote measurements under various weather conditions. To avoid damage from smaller rocks and debris, critical surfaces are often protected by rockfall catch fences. We present an experimental investigation proving that the radar measurements are indeed significantly affected by a catch fence made of steel even if its mesh size is larger compared to that of the wavelength of the radar. A stable rock wall in a quarry was monitored by means of a ground-based synthetic aperture radar for 2 days. Different fences varying in shape, size, and density of mesh and in various geometrical configurations were erected at different locations for short periods of time during the experiment. We show that for surfaces observed through the fence, the reflected power can be reduced by 20 dB and thus the signal-to-noise ratio is significantly deteriorated. We also observed spurious interferometric phase shifts. Even parts of the rock wall not covered by the fences are affected. Side lobes and mixed pixels result, e.g., in severe loss of coherence and thus potentially mask actual displacements.

Keywords GB-SAR · Terrestrial radar interferometry · Rockfall · Protection fence · Natural hazards

Introduction

A crucial part of each early-warning system is reliable and accurate displacement and deformation monitoring. This can be achieved, e.g., by using data from sensors like fiber Bragg grating (Huang et al. 2012), inclinometers and extensometers (Wyllie and Mah 2004), geodetic monitoring by means of robotic total stations (Loew et al. 2012; Frukacz et al. 2016), global positioning systems (Crosta and Agliardi 2003) or remote sensing methods like digital photogrammetry (Di Crescenzo and Santo 2007), terrestrial laser scanning (Rabatel et al. 2008; Gigli et al. 2014), and terrestrial radar interferometry (TRI). The latter shows a great potential to provide highly accurate data and thus high sensitivity with respect to deformation of observed natural objects (Mazzanti 2011, Monserrat et al. 2014).

A radar sensor emits electromagnetic waves and receives signals reflected from the surfaces generating a 2D complex image with phase and amplitude information for every radar pixel. Range resolution is obtained by the frequency modulation of the emitted signals, and azimuth resolution is generated by moving the antennas along a rail (synthetic aperture) or rotating real aperture antennas. All targets located in the same azimuth-range bin contribute to the amplitude and phase value of the same pixel. Forming an interferogram of two radar images of the same area and collected at different times, the interferometric phase as a measure of displacement along the respective line-of-sight (LOS) can be obtained (Rödelsperger 2011, p18). The TRI sensor can be installed in a stable and safe location several kilometers from the monitored area. High accuracy (below 1 mm) and sampling rate (1–5 min depending on the sensor) make TRI suitable for applications demanding quasi-areal and near real-time displacement information under a broad range of meteorological conditions. Actually, TRI is now widely applied for deformation monitoring, in particular for monitoring landslides (Antonello et al. 2003; Mazzanti et al. 2014), open pit mine fields (Severin et al. 2011), snow covered slopes and glaciers (Luzi et al. 2009; Butt et al. 2016a), volcanoes (Intrieri et al. 2013), and rockfalls (Rabatel et al. 2008; Miller et al. 2013). One of the key challenges is a successful mitigation of atmospheric effects, which may completely mask the actual displacement (Luzi et al. 2004; Butt et al. 2016b). Additionally, TRI data interpretation can be difficult because of the geometric distortions involved in mapping 3D space onto the 2D azimuth-range space (Rödelsperger 2011; Monserrat et al. 2014). Due to the LOS nature of TRI sensitivity, prior knowledge of the expected deformation is needed for proper selection of the instrument location. Low coherence (e.g., due to vegetation) and ambiguous interferometric phase (e.g., due to fast large displacements) are further limiting factors.

If a hazard zone reaches an infrastructure or habitat area, special protective structures (embankments, ditches, sheds, galleries, or fences) may be installed independently from a potential monitoring system (Volkwein et al. 2011). Steel fences (e.g., Coates et al. 2006) are often found in real hazard zones because of their relatively low-cost, quick-installation and low-impact characteristics on the landscape (transparency). While they can prevent a damage caused by certain actual events, they may disturb or invalidate TRI monitoring. Firstly, the solid parts of the fences and their support are obstacles in the LOS, non-transparent for microwaves. They cause shading of parts of the surface to be monitored, thus, potentially masking changes of these areas (Fig. 1). Typically, the mesh size of the fence is much bigger than the wavelength of the radar and the physically shaded area is less or much less than 25% of each affected azimuth-range bin. Secondly, steel has much higher reflectivity for microwaves (about 99%) than natural surfaces (e.g., 30% for sedimentary rock; see Ulaby et al. 1990; Gupta and Wong 2007, chapter 4). It is known that the presence of highly reflective targets in the observed scene may produce side lobes which can interfere with the signal of other less reflective objects (Rödelsperger 2011, p.13). Thus, the steel fence can additionally mask deformation signals even in areas not shaded by the fence. It can also be expected that a fence located in the same azimuth-range bin as an observed natural surface may become a dominant scatterer, therefore, again masking actual deformation of the other surfaces.

As the reflected power of a radar wave is characterized by the radar cross section (RCS), which is a function of angular orientation, shape, and electromagnetic properties (electric permittivity and magnetic permeability) of the scattering body, as well as frequency and polarization of the emitted wave (Skolnik 1990,

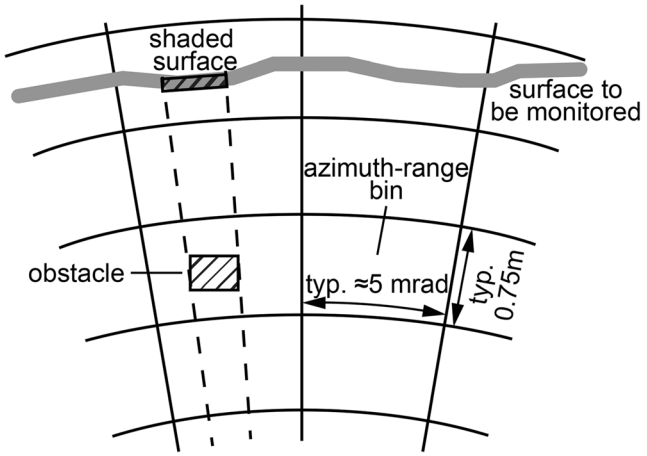

Fig. 1 Monitoring by means of terrestrial radar interferometry with an obstacle between the radar and the surface to be monitored

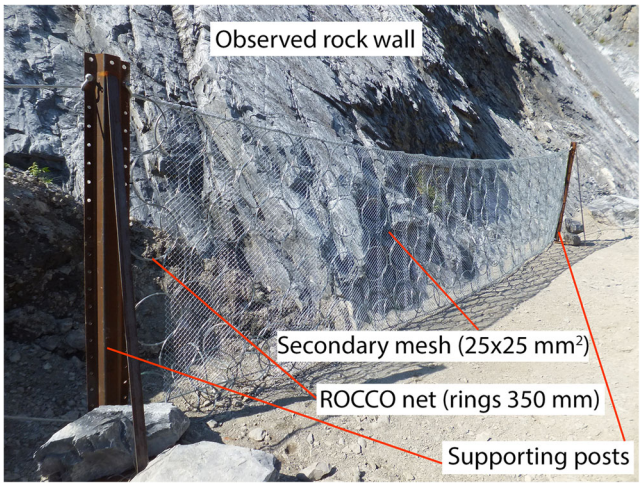

Fig. 2 Experimental setup in scenario 4: two posts located close to the rock wall, supported by stones and wires, with attached ROCCO fence plus secondary mesh

chapter 11; Knott et al. 2004, chapter 3), analytical modeling of such an impact is hardly possible and practically useful numerical simulations are very difficult to realize (Franceschetti et al. 1992). For this reason, the investigation was carried out experimentally. Herein, we present an analysis indicating qualitatively and quantitatively the potentially detrimental impacts of rockfall catch fences on TRI with synthetic aperture. We focus on amplitude, coherence, and phase of radar interferometry and analyze the most critical parameters of the rock-fence-sensor geometry.

Methods and experimental setup

Measurements were collected during 2 days in a quarry, with the instrument set up at a distance of about 90 m from a rock wall. The instrument was not moved during this period, and the rock wall was supposed to be stable. So, all apparent displacements of the rock wall later obtained from the measurement data were interpreted as deviations.

Two types of fences were erected temporarily between the instrument and the rock wall: (i) a ring net[1] consisting of circular rings with a diameter of 350 mm each, made from seven windings of steel wires (3-mm diameter per wire, 9-mm diameter of bundle), and (ii) a secondary steel mesh with square meshes of about 25×25 mm^2 made from steel wires with a 2-mm diameter. These fences were set up approximately vertically at an azimuth corresponding to the strike direction of the rock wall. They were supported by posts[2], 2 m high and 10 m apart, that were in turn stabilized by steel wires and by stones around their bottom ends, see Fig. 2.

The chosen radar instrument[3] was a ground-based radar interferometer operating in the Ku band (central frequency f = 17.2 GHz, central wavelength $\lambda \approx 17$ mm) with a bandwidth of 200 MHz and thus a depth resolution of 0.75 m. Its cross-range resolution of 4.4 mrad results from a synthetic aperture with the radar head moving along a linear rail of 2 m in length. One data acquisition—yielding ultimately a single-look complex image (SLC)—required about 5 min. An antenna with a gain of 14 dBi, a horizontal beam width of 29° and a vertical one of 25°, was chosen as a tradeoff between the illuminated area and power of the reflected signal. The system and its properties for geomonitoring are discussed comprehensively in (Farina et al. 2011; Rödelsperger 2011).

Radar data were initially collected without any artificial objects between the instrument and the rock wall for reference. This was repeated at the very end of the experiment. In between, various combinations of posts, primary, and secondary net were set up in different positions. Each of these configurations represents a distinct scenario as reported in Table 1, and for each of them, a series of data acquisitions has been carried out starting one immediately after the previous one that had been completed. This resulted in the availability of typically five, sometimes more or less, SLCs about 5 min apart per scenario.

For each scenario, the entire setup comprising radar instrument, fences, posts, and rock wall was scanned using a terrestrial laser scanner. The surface model obtained from one such scan was later used to display the radar results by projecting from azimuth-range bins onto a 3D surface model. Furthermore, using these data allowed determining exactly the location of the fences and posts within the radar image and thus better analyzing their impact both on areas of the rock wall monitored through the fence and on areas far away from the fence.

For each scenario, the impact of the fences on the monitoring of the rock wall was investigated by comparing power (amplitude image), coherence, and phase to the values obtained from the reference scenario. Furthermore, the variability of each of these parameters within the individual scenario was also analyzed and taken into account when assessing the impact of the fence.

Data processing

The SLCs were produced from the raw data files of the corresponding data acquisition by focusing in range (r) and cross-range direction (α). Further processing of these complex images was performed using proprietary Matlab tools, in particular, for calculating phase and amplitude per pixel and for deriving the interferograms between pairs of SLCs by pointwise multiplication

[1] Geobrugg ROCCO ring net type 7/3/350
[2] Geobrugg GBE-100A-R
[3] IBIS-FM, IDS Ingegneria dei Sistemi, with IBIS-ANT2 antenna

Table 1 Summary of scenarios

Scenario	Support		Fence		Distance from wall [m]	SLCs	Start time [day, h:mm]	Comments
	Posts	Stones	ROCCO	Secondary				
1						9	1, 11:34	
2	X				0.2–1.0	5	1, 12:43	
3	X	X	X		0.2–1.0	5	1, 14:57	
4	X	X	X	X	0.2–1.0	5	1, 16:21	
5	X	X	X	X	0.2–1.0	6	1, 17:14	Middle part of the fence shifted about 0.2 m towards the instrument
6	X	X			0.2–1.0	5	2, 9:14	
7	X	X			6.5–7.5	5	2, 10:02	
8	X	X	X		6.5–7.5	5	2, 10:59	
9	X	X	X	X	6.5–7.5	5	2, 12:09	
10	X	X	X	X	6.5–7.5	5	2, 12:46	Middle part of the fence shifted about 0.2 m towards the instrument
11	X	X	X	X	6.5–7.5	2	2, 13:26	
12	X	X	X	X	6.5–7.5	2	2, 13:44	
13	X	X	X	X	6.5–7.5	2	2, 14:01	
14		X				10	2, 14:55	

of the complex numbers. The interferometric phase ($\Delta\phi_m$), i.e., the phase change per azimuth-range bin, the coherence as a quality indicator of the interferograms, and the amplitudes were then used for the analysis. The applied processing chain is shown in Fig. 3.

For all grid cells (r,α) expressed in a local coordinate system of the radar and for all pairs of times t_i and t_j, the measured interferometric phase $\Delta\phi_m$ can be expressed as (after Noferini et al. 2005; Kampes 2006):

$$\Delta\phi_m(r,\alpha,t_i,t_j) = \Delta\phi_{\text{defo}}(r,\alpha,t_i,t_j) + \Delta\phi_{\text{atmo}}(r,\alpha,t_i,t_j) + \Delta\phi_{\text{noise}}(r,\alpha,t_i,t_j) \quad (1)$$

where $\Delta\phi_{\text{defo}}$ is the phase due to the real deformation expressed as differential surface displacement along the look direction, $\Delta\phi_{\text{atmo}}$ is the contribution of the atmosphere, and $\Delta\phi_{\text{noise}}$ is the random noise (decorrelation noise). The influence of the topography, which is typically included in this equation for satellite-based radar interferometry, has already been omitted here because it does not show up in ground-based radar interferometry with the instrument set up at a fixed location.

Assuming that the relative humidity has values between 20 and 90%, air temperature is between 15 and 25 °C, and barometric pressure is between 940 and 980 mbar, variations of the refractive index during the experiment can cause apparent LOS distance changes up to 106 ppm (according to the formulas proposed by Rüeger 2002). This corresponds to apparent phase changes of more than 520° in this experimental setup where the distances are up to 120 m. The expected noise level and the resolution of the radar system are on the order of a few degrees. So, atmospheric corrections are needed before analyzing the impact of the fence.[4] However, it is not possible to measure the atmospheric parameters with sufficient accuracy, spatial and temporal resolution on site or to predict them with sufficient accuracy using a peripheral model of meteorological corrections. Therefore, permanent scatterers (PS) (e.g., Ferretti et al. 2001; Kampes 2006) within stable areas of the monitored scene, i.e., scatterers with high coherence during the experiment and not affected by the fences and their support, were used to mitigate the atmospheric impact. Ferretti et al. (2001) have proposed to identify permanent scatterer candidates (PSC) using the amplitude dispersion index (ADI) $I_A(r,\alpha) = \sigma_A(r,\alpha)/m_A(r,\alpha)$, where σ_A and m_A are the standard deviation and mean of the amplitude A of a certain pixel (r,α) across a certain stack of SLCs, i.e., during a chosen period of time. A low ADI indicates potentially high coherence and a high signal-to-noise ratio (SNR), which are prerequisites for accurate differential phase measurements. Using a threshold even more stringent than the ones proposed in Ferretti et al. (2001), we have chosen pixels with an ADI less than 0.07 as PSC. It was reasonable to select such a low value because the ADI is generally much lower with low distance and strong reflectors in terrestrial radar interferometry than that with the typical space-born SAR interferometry. Most of the selected PSC indeed show high coherence, but for some, the minimum coherence within the experiment was lower than 0.8 (reaching even 0.3); therefore, we decided to apply an additional threshold and only select pixels with a coherence

[4] The meteorological values actually observed during the measurements varied less, but the atmospheric phase screen variations computed from the actual values were still close to 90° and thus relevant.

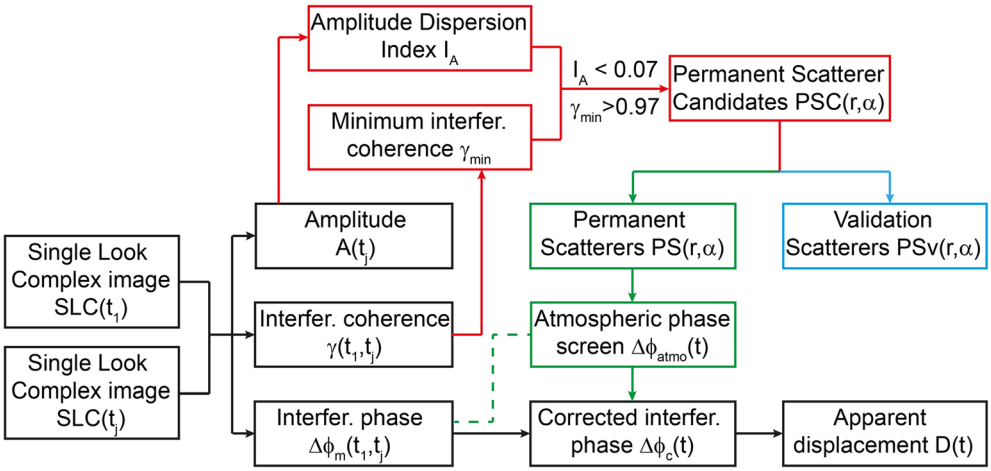

Fig. 3 Flow chart depicting the processing steps

higher than 0.97. In total, 269 PSC resulted from this selection. We chose 80 of them, located in the area of interest later to be analyzed, as validation scatterers (PSv) for subsequent assessment of the atmospheric corrections (Fig. 4). The remaining 189 PSC, located outside the area of interest and assumed to be stable and unaffected by the fences, were used as the PS for atmospheric phase screen (APS) calculation.

It is usually assumed that the APS varies linearly with range between sensor and target (Noferini et al. 2005; Rödelsperger 2011, p.32), but we also observed a dependence on azimuth. Assuming that the atmospheric contribution can be modeled as a bivariate polynomial of low degree in range and azimuth with coefficients depending on time, we have:

$$\Delta\phi^{\mathrm{mod}}_{\mathrm{atmo}}(r,\alpha,t) := \sum_{i,j} a_{ij}(t)\cdot r^i\cdot\alpha^j \qquad (2)$$

For simplicity, we write only one time argument, henceforth, omitting the explicit indication of the reference time, which for the whole analysis, was the first SLC. In our case, it was sufficient to choose bilinear interpolation, i.e., $i \le 1$ and $j \le 1$ (higher coefficients were rejected as not significant).

The unknown coefficients $a_{ij}(t)$ in this model were estimated independently for each time from the measured interferometric phase values at the PS, which can be considered direct observations of the APS at the corresponding pixels and times:

$$\Delta\phi_m(r_{\mathrm{PSi}},\alpha_{\mathrm{PSi}},t) = \Delta\phi_{\mathrm{atmo}}(r_{\mathrm{PSi}},\alpha_{\mathrm{PSi}},t) + \phi_{\mathrm{noise}}(r_{\mathrm{PSi}},\alpha_{\mathrm{PSi}},t) \qquad (3)$$

In our case, the four parameters of the model were estimated from the 189 interferometric phase values at the PS using least squares adjustment of these highly redundant observations. The estimated coefficients $\hat{a}_{ij}(t)$ are then used to interpolate the atmospheric phase for all pixels of the radar image and subtract this interpolation from the measurements according to:

$$\begin{aligned}\Delta\phi_c(r,\alpha,t) &:= \Delta\phi_m(r,\alpha,t) - \Delta\phi^{\mathrm{mod}}_{\mathrm{atmo}}(r,\alpha,t)\\ &= \Delta\phi_m(r,\alpha,t) - \sum_{i,j} a_{ij}(t)\cdot r^i\cdot\alpha^j \end{aligned} \qquad (4)$$

where $\Delta\phi_c$ is the corrected interferometric phase. The latter can be converted into an apparent metric displacement D (change in distance between the radar sensor and scatterer) for each pixel and all times:

$$D(r,\alpha,t) = \Delta\phi_c(r,\alpha,t)\frac{\lambda}{4\pi} \qquad (5)$$

The quality of the corrected interferometric phase after APS mitigation was assessed using time series of interferometric phase of each PSv converted to D. The standard deviation of these time series was in the range of 0.03–0.10 mm depending on the respective scatterer. These values are on the order of the noise level of the radar instrument. In Fig. 5, originally measured (blue) and atmospherically corrected (red) interferometric phases are shown as apparent displacement for one representative PSv. The APS was successfully mitigated from the phase information and there is good agreement of the obtained results with specified sensor accuracy of 0.1 mm.

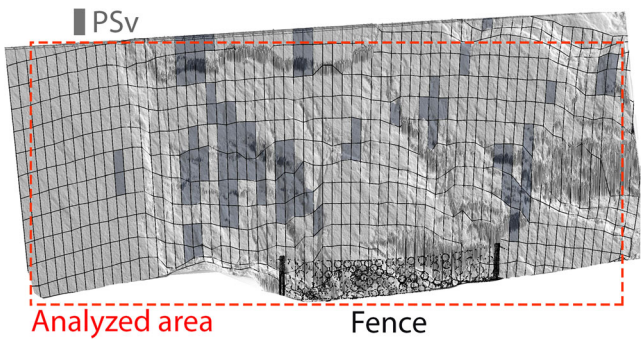

Fig. 4 Persistent scatterers used for validation (PSv, *dark-gray*) of the atmospheric effects, displayed on digital model of the rock wall with azimuth-range bins indicated by grid lines and fence as set up during scenario 3

Analysis

The further investigation was carried out by analyzing the time series of power, coherence, and phase of each pixel in the stack of atmospherically corrected interferograms related to the reference SLC. From the set of 14 scenarios, three (11–13) were excluded because only two acquisitions had been performed for each of these scenarios. We present the key results using only six pixels,

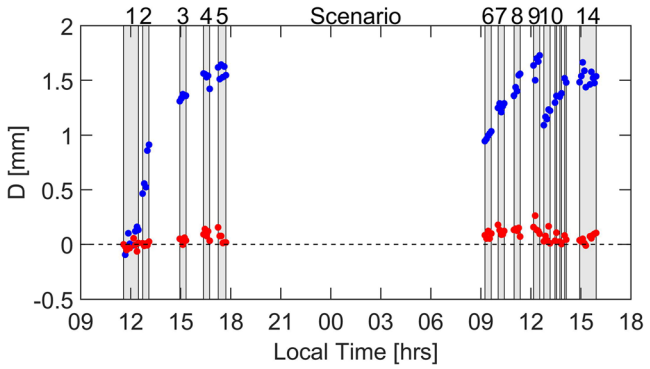

Fig. 5 Apparent displacement of a selected PSv without (*blue*) and with (*red*) APS correction

each of them representative of a specific group of pixels in the whole image (Fig. 6). One of the PSv (pixel 1) was selected to demonstrate the small variability of analyzed parameters for the persistent scatterers. Most of the pixels located on the rock wall show a similar behavior to the PS and PSv, but the observed changes are slightly larger. At the same time, there are some points located on the rock wall showing different effects than for the PS; therefore, two of them were selected (pixels 2 and 3) to present these anomalies. One pixel located on the stable pile of gravel in the same range as the fence but different azimuth was chosen (4) to show the impact of strong side lobes. Critical areas of the rock wall observed through the fence (the same azimuth and elevation as the fence) are represented by the last two pixels: no. 5 is located in a different range bin than the that of the fence and pixel no. 6 is located in the same range bin as that of the fence in scenarios 3–5 (so-called mixed pixel), but in a different range bin in scenarios 8–13, when the fence was moved away from the rock wall.

Changes of the reflected power

Although phase is the most important information in the SLCs used for interferometry, also the amplitude is crucial. It determines the signal-to-noise ratio, an indicator of the quality of the interferogram. For convenient quantification of vastly different values, we will subsequently assess the power ratio (expressed in dB), i.e., $P = 20\log_{10}(A/A_r)$ with respect to a reference value A_r (given by the radar processing software) instead of the amplitude. As expected, during focusing, power reflected by highly reflective fences spreads to adjacent pixels, masks signals of other less reflective targets, and produces side lobes due to the finite length of the synthetic aperture (Fig. 7). The side lobes are visible as high power for all pixels with the same range as the fence (i.e., circular arcs in Fig. 7b) while in reality most of the pixels at this range correspond to only weakly reflecting surfaces (see Fig. 7a).

The differences ΔP of the received power (which are independent of A_r) with respect to the average power of the corresponding pixels during the first scenario (no fences) were calculated for each pixel. They are summarized in Fig. 8. For all PS and PSv pixels, the reflected power remains almost constant during the whole experiment; the variations within scenarios are mostly smaller than 1 dB, and during the whole experiment, the maximum difference between the lowest and highest reflected power of any PS and PSv was 3.5 dB. Most of the pixels located on the rock wall show similar pattern but slightly a wider range of power variations. The reflected power from pixels in the rough, irregular surface located above and to the right of the fence is in the range of 2–5 dB (similar azimuth but different range). Pixel 2 and others located on the almost planar, smooth rock face to the left of the fence show higher variability within scenarios and over the whole experiment (range typically 5–10 dB). For most of these pixels, no relation between the observed changes and the presence of the fences can be observed. The reflected power of pixel 3 reduces by about 10 dB during the first scenarios. The pixel corresponds to a shallow recess of the rock wall. The effect can be mostly explained by the slow drying of the rock after the rainy day when the experiment was started (resulting in a change of −5 dB between the first and last scenarios). This decreasing trend on the reflectivity is visible for some other pixels as well especially during the first sunny day of the experiment, when the rock moisture content was decreasing and thus the dielectric loss factor (Ulaby et al. 1990). It can also be observed that in scenarios with the fence close to the wall, the noise in the reflected power is higher than those in other scenarios even for pixels located in different range and azimuth bins than those of the fence.

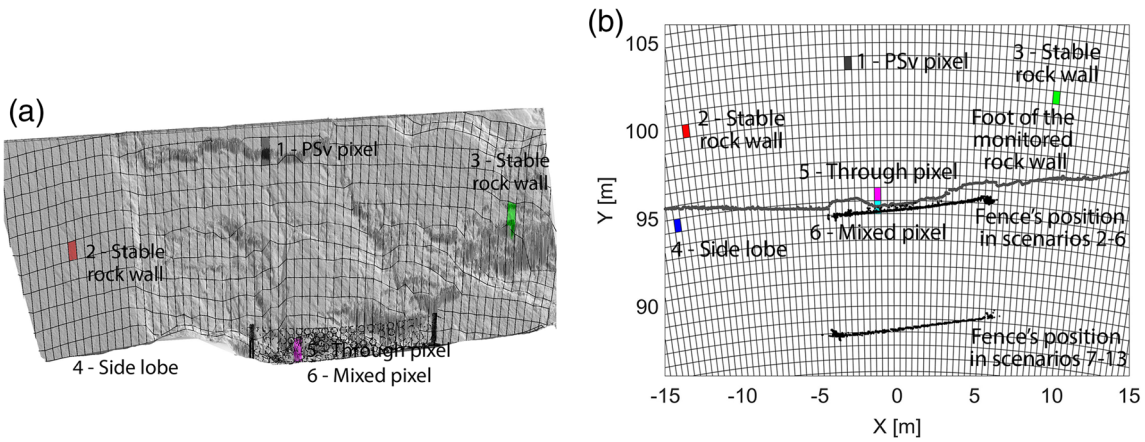

Fig. 6 Selected radar pixels projected onto the digital terrain model of the rock wall as seen from the radar point-of-view (**a**) and plane view of the experimental setup (**b**) in local coordinate system centered at the radar (0, 0)

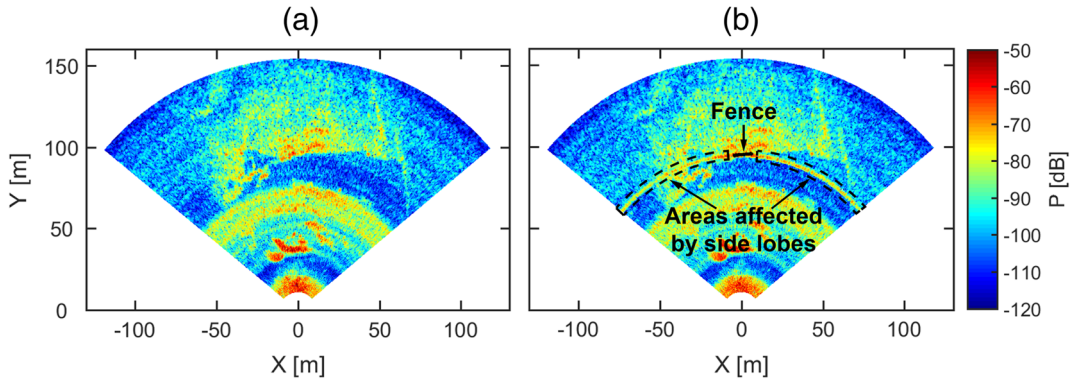

Fig. 7 The power map of the scenario without any fence (SLC 1, (**a**)) and a scenario with the fence located close to the rock wall (SLC 25, (**b**))

As it was expected, pixels observed through the fence but located in a different range bin (e.g., pixel 5 in all scenarios with the fence, pixel 6 in scenarios with the fence at the greater distance from the rock wall) have reduced power, as the fence acts as a reflector for part of the microwave radiation. The attenuation of the reflected power in areas shaded by the fence is stronger with the denser fence (−10 dB) than that just with the Rocco fence (−5 dB). However, there are some times with more than 20 dB attenuation. In scenarios with the fences close to the rock wall, the changes are bigger and noisier than those in the scenarios with the fences at a greater distance from the rock, when that damping effect of the ROCCO fence is even smaller. There is no clear pattern in scenarios with the fence slightly shifted in the middle (scenarios 5 and 10), but the variations of the reflected power are usually noisier with possible outliers. For parts of the rock wall located in the same azimuth-range bins as the fence (mixed-pixels, e.g., 6), power gains exceeding 10–15 dB can be observed in scenarios with the fence close to the rock wall (scenarios 3–5). For pixels located in the side lobe (e.g., pixel 4), which is 3–4-range-bin wide, this gain in power can be even bigger (more than 20 dB). This phenomenon can be explained by lower initial amplitude of these pixels (reflection from the pile of gravel, not the solid rock).

Coherence

The coherence can be calculated for each pixel (r,α) of the complex interferogram according to (Hanssen 2002, p.96).

$$\gamma_{r,\alpha}(t_1,t_2)=\frac{E\left\{y_{r,\alpha}(t_1)y^{*}_{r,\alpha}(t_2)\right\}}{\sqrt{E\left\{\left|y_{r,\alpha}(t_1)\right|^2\right\}E\left\{\left|y_{r,\alpha}(t_2)\right|^2\right\}}},\ 0\le\gamma_{r,\alpha}(t_1,t_2)\le 1 \quad (6)$$

where $y_{r,\alpha}(t)$ and $y^{*}_{r,\alpha}(t)$ are the complex values at time t and its complex conjugate, and $E\{\cdot\}$ is the expectation operator

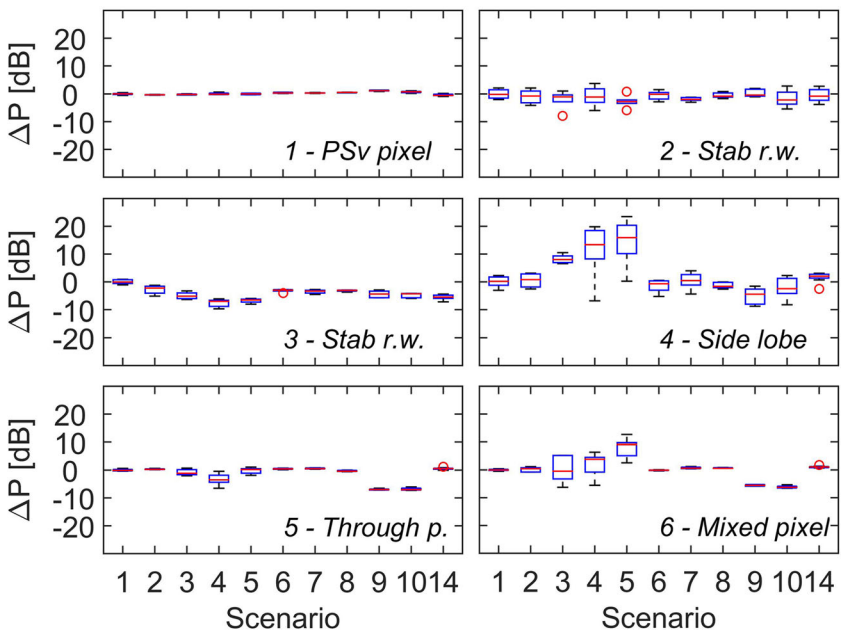

Fig. 8 Difference of the reflected power with respect to the mean of scenario 1 for the selected pixels (standard boxplot)

yielding the corresponding mean values of the stochastic processes. It is used to assess the accuracy of the interferometric phase according to (Bamler and Hartl 1998).

$$\sigma^2_{\Delta\phi_{ij}} = \frac{\pi^2}{3} - \pi\arcsin\left(\left|\gamma_{ij}\right|\right) + \arcsin^2\left(\left|\gamma_{ij}\right|\right) - \frac{\mathrm{Li}_2\left(\left|\gamma_{ij}\right|^2\right)}{2}\,[\mathrm{rad}] \quad (7)$$

where $\mathrm{Li}_2(\cdot)$ is Euler's dilogarithm. Usually, the expectations in Eq. 6 are replaced by spatial averages obtained over an estimation window of N pixels surrounding the pixel of interest to calculate the maximum likelihood estimator of the coherence (Seymour and Cumming 1994; Hanssen 2002). In our experiment, variations of the reflected power in regions close to or observed through the fence lead to changes of the SNR thus to local variations of the phase accuracy; therefore, spatial averaging introduces these variations into neighboring pixels and mitigates these variations for affected pixels, resulting in a spatiotemporal coherence (Fig. 9). This effect can be observed, e.g., for pixels 5 and 6 located next to each other; anticipated significant variations of coherence of the mixed pixel due to a spatial averaging are also present (in an attenuated form) for pixel 5.

In case of our analysis, each scenario has at least 5 acquisitions with all measurements collected within a very short time window (25 min) and thus under almost identical atmospheric and geometric conditions. Therefore, we have chosen two strictly temporal coherences calculated pixel by pixel: coherence (a) of each scenario with respect to scenario 1 and (b) within each scenario. The former temporal coherence γ_T can be estimated for each pixel (r,α) and each scenario s_k using p corresponding pairs of SLC images from scenario 1 and k with:

$$\left|\gamma_{Tr,\alpha}(s_1, s_k)\right| = \frac{\left|\sum_{n=1}^{p} y_{r,\alpha}(s_{1,n})\, y^*_{r,\alpha}(s_{k,n})\right|}{\sqrt{\sum_{n=1}^{p}\left|y_{r,\alpha}(s_{1,n})\right|^2 \sum_{n=1}^{p}\left|y_{r,\alpha}(s_{k,n})\right|^2}} \quad (8)$$

where $y_{r,\alpha}(s_{k,n})$ is the complex value of pixel (r,α) of the n-th SLC in scenario s_k. The temporal coherence γ_S within each scenario s_k can be calculated using $m-1$ pairs of subsequent SLC images with m being the number of SLCs in the scenario:

$$\left|\gamma_{Sr,\alpha}(s_k)\right| = \frac{\left|\sum_{n=1}^{m-1} y_{r,\alpha}(s_{k,n})\, y^*_{r,\alpha}(s_{k,n+1})\right|}{\sqrt{\sum_{n=1}^{m-1}\left|y_{r,\alpha}(s_{k,n})\right|^2 \sum_{n=1}^{m-1}\left|y_{r,\alpha}(s_{k,n+1})\right|^2}} \quad (9)$$

With both temporal coherences, the spatial averaging is omitted and coherence of each pixel can be calculated and interpreted independently (Fig. 10). For most of the pixels, no significant temporal decorrelation can be observed between scenarios 1 and 14, i.e., between the two scenarios without any fences and posts but separated by about 27 h. Also, the internal coherence within both scenarios for those points is high (almost 1). It indicates that all systematic effects were successfully mitigated, and variations visible for other scenarios are caused by the presence of the fences. Two pixels show lower coherence (about 0.9) within the last scenario—pixel 2 located on the smooth rock-face and pixel 4 located on the pile of gravel. This confirms that those pixels have worse scattering properties than the others. The reduced temporal coherence in scenario 14 with respect to the first scenario of pixel 3 is very likely linked to the above mentioned drying of that part of the rock wall. The temporal coherence is significantly reduced for mixed and side lobe pixels within scenarios with the fences close to the rock wall and reaches 0.2–0.4, which corresponds (according to Eq. 7) to standard deviations of the interferometric phase of about 80°to 90°. It is striking that even for scenario 2 (posts without any fence), the coherence of pixel 4 is already low, although for this scenario, the side lobe effect was not clearly visible in the power analysis. The low coherence indicates that pixels

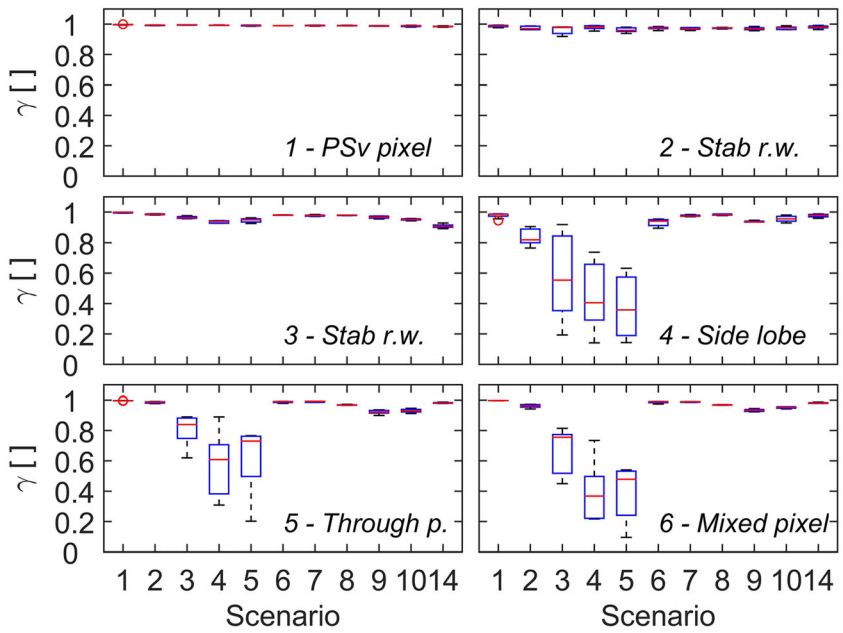

Fig. 9 The spatiotemporal coherence calculated with a spatial window of 3 × 3 pixels (standard boxplot)

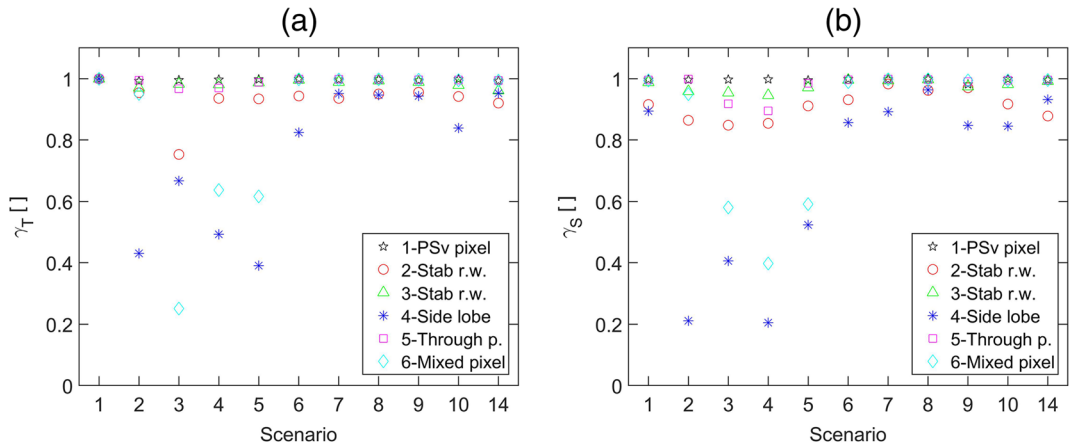

Fig. 10 Temporal coherence of selected pixels (**a**) related to the 1st scenario and (**b**) within scenarios

containing fences or located in the side lobes should not be used for deformation analysis. For points observed through the fence as well as some points located on the rock wall, we can observe reduced coherence within scenarios with the fences close to the rock wall, while this effect is not visible with the fences located in a greater distance from the rock wall. It can be seen that the coherence within scenario 4 for pixel 5 is reduced to 0.9; so, the standard deviation of the interferometric phase is increased by a factor of about 2 (40° instead of 20°). Such a decorrelation means that the corresponding pixels show higher phase variations and the deformation monitoring can be less sensitive with respect to small displacements in such pixels.

Interferometric phase and apparent displacement

As discussed above, the expected interferometric phase of pixels located on the rock face should be equal to 0°. We have shown in chapter 3 that this indeed holds for all PSv for all times. For pixels located on the rock wall but not selected as permanent scatterers, we at least expected to observe no significant apparent displacement between scenarios 1 and 14, both measured without any fences and a day apart. The actually observed displacements for more than 90% of these pixels were in the range of ±1 mm, which corresponds to $2{\cdot}\sigma_{\Delta\phi c}$ based on a coherence of 0.98. The remaining pixels show higher interferometric phase variations and lower coherence in scenario 14, which is likely explained by changing or worse scattering properties of these pixels (drying and smoothness of the rock wall). These pixels were removed from further calculations and are shown in white in Fig. 11, which depicts the apparent displacement maps for three selected scenarios, while Fig. 12 shows that for all analyzed scenarios but for selected pixels only.

The interferometric phase and apparent displacement of selected pixels in the first and last scenario are similar. Small variations within these scenarios can be observed with the exception of two selected pixels (pixel 2 on smooth rock-face, pixel 4 on the pile of gravel). All selected pixels but pixel 1 show higher phase variations in scenarios 3–5 with the fence located close to the rock wall, which is explained by deteriorated coherence, thus bigger standard deviation of the interferometric phase. This effect is extreme for side lobe and mixed pixels; virtually total temporal decorrelation leads to interferometric phase variations up to ±180° and apparent displacements up to ±4.4 mm. This means that displacements in these areas are not observable using the radar instrument. Parts of the rock wall observed through the fence located in a greater distance from the wall (pixel 5 and pixel 6 in scenarios 8–10) have a small phase standard deviation but show a systematic shift (up to 80°)

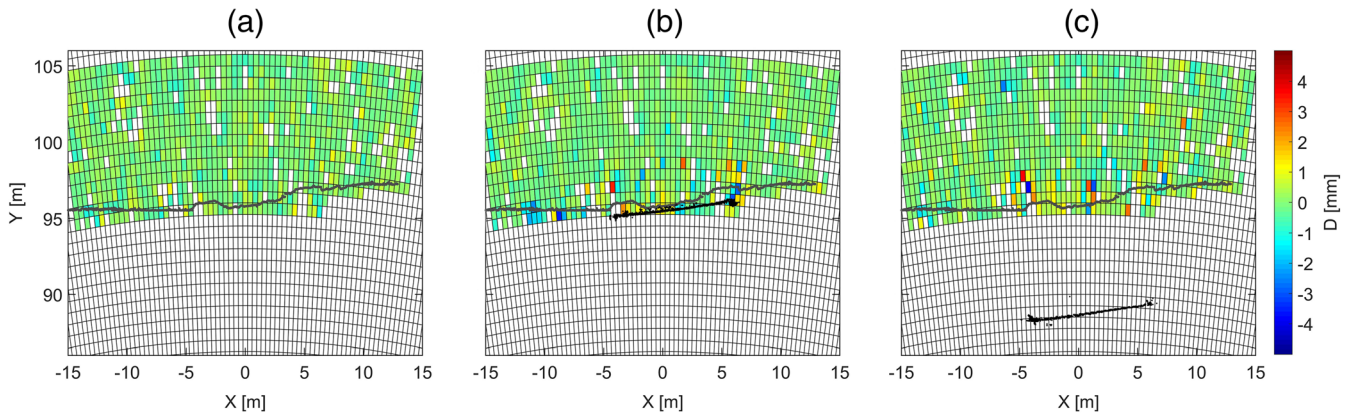

Fig. 11 Radar maps of mean apparent displacement D [mm] (calculated using Eq. 5 and then averaged within each scenario): (**a**) scenario 14 without any fences between the radar and the rock wall, (**b**) scenario 5 with the fences close to the rock wall, and (**c**) scenario 9 with the fences at about 7 m from the rock wall

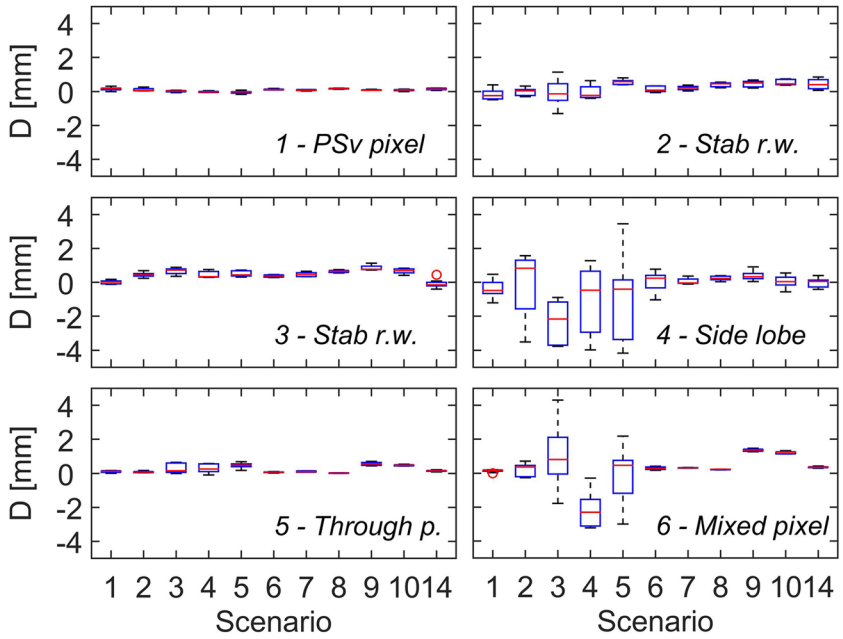

Fig. 12 Apparent displacement (calculated using Eq. 5) of the selected pixels (standard boxplot)

caused especially by the presence of the denser secondary fence. This apparent displacement of pixels observed through the fence located close to the rock wall is still visible but may be masked by the higher phase noise (e.g., pixel 5 in scenarios 3–5). For pixels located in different azimuth-range bins than the fence (e.g., pixel 3), we can still observe small phase shifts in scenarios with the fence in the radar field-of-view. We have not selected pixels showing extreme effects visible (e.g., in Fig. 11 right), where one can identify pixels observed through the fence with measured apparent displacement of about 4 mm. A different sign of displacements for neighboring pixels is likely related to unsolved phase ambiguity when displacement exceeds 180°. Another phenomenon visible in Fig. 11 for scenarios with fences is the presence of strong apparent displacements of pixels located in the same or similar azimuth bins than the posts supporting the fence. This effect can be observed even for pixels in different range bins and not covered by the posts and might suggest the presence of longitudinal lobes produced during focusing in range with finite bandwidth (compare to chapter 4.1), but not visible in the power maps.

Conclusions and outlook

The presence of a rockfall catch fence in an area monitored by a ground-based synthetic aperture radar (GB-SAR) can be highly detrimental for the monitoring results even if the mesh size of the fence is much bigger than that of the wavelength. We have shown and analyzed this using an experimental investigation employing an IBIS-FM GB-SAR instrument with a wavelength of 17.5 mm, a fence with circular rings with a diameter of 350 mm, and a fence with a square mesh of 25 × 25 mm2. The data were processed by interferometry starting from single-look complex images with atmospheric phase screen mitigation based on persistent scatterers and spatial interpolation at each time.

As expected, the most critical configuration is when the fence is located in the same range and also azimuth bins as the observed surface (for example if the fence is directly attached to the rock). In these cases, the reflected power can be increased by more than 15 dB and the coherence reduced down to 0.2. Consequently, the interferometric phase information is not reliable (the corresponding standard deviation can reach or even exceed 90°) and the surface displacement cannot be observed using the radar interferometer. Similar effects were found for pixels located in side lobes produced during the synthetic aperture processing. We have again found reduction of coherence down to 0.2 while the gain of the reflected power exceeded even 20 dB. In such cases, the interferometric phase variations can be up to ±180°; therefore, the phase carries no more displacement information, and consequently the observed apparent displacements may be unrelated to the true ones.

For pixels observed through the fence but located in different range bins, the reflected power was reduced by about 5–10 dB and the measured apparent displacement was up to 2 mm. With just slightly deteriorated coherence (0.90–0.95 depending on the scenario), the measurements of displacement are systematically affected but probably deriving sufficiently accurate velocity estimates may be still possible. This will be a subject for future research.

Additionally, in the scenarios with the fences, we observed deteriorated signal-to-noise ratio, lower coherence (0.8) and interferometric phase shifts exceeding 40° for some pixels not measured through the fence and located in different range bins. These effects were particularly large for pixels located in the same azimuth bins as the fence or supporting posts. They are due to longitudinal lobes arising from the range focusing.

Based on results of our investigation, we recommend to avoid monitoring of surfaces by means of GB-SAR in the presence of highly reflective fences in the line-of-sight of the radar. If this cannot be avoided, special attention is needed for parts of the monitored surface located in the same range and azimuth bins as

the fences or affected by the side lobes, as their displacement cannot be reliably observed. In such cases, an additional monitoring technique for these areas is recommended. Special caution should also be exercised while interpreting the monitoring results of pixels observed through the fence as they might be systematically affected and show higher standard deviation.

Further investigations are planned to (i) compare the effect of the fence on GB-SAR to terrestrial radar interferometry with a real aperture and (ii) to verify experimentally that monitoring of objects behind the fence but in different range bins is possible and mainly affected in terms of increased noise level.

Acknowledgements

Dr. Lorenz Meier, Geopraevent AG, has motivated the investigation, provided the radar instrument, and supported the authors during data processing. Geobrugg AG (Dr. Corinna Wendeler) has provided the fences and supported during the measurements.

References

Antonello G, Casagli N, Farina P, Fortuny J, Leva D, Nico G, Sieber AJ, Tarchi D (2003) A ground-based interferometer for the safety monitoring of landslides and structural deformations. Geosci Remote Sens Symp 2003 IGARSS'03 Proceedings 2003 I.E. Int Vol 1 218–220

Bamler R, Hartl P (1998) Synthetic aperture radar interferometry. Inverse Probl 14:R1–R54. doi:10.1088/0266-5611/14/4/001

Butt J, Conzett S, Funk M, Wieser A (2016a) Terrestrial radar interferometry for monitoring dangerous alpine glaciers: challenges and solutions. In: Proceedings of GeoMonitoring 2016 Braunschweig. pp 69–87

Butt J, Wieser A, Conzett S (2016b) Intrinsic random functions for mitigation of atmospheric effects in ground based radar interferometry. In: Proceedings of JISDM 2016 Vienna

Coates R, Bull G, Glisson F, Roth A (2006) Highly flexible catch fences and high performance drape mesh systems for rockfall protection in open pit operations. In: Villaescusa E, Potvin Y (eds) Ground support in mining and underground construction. Taylor & Francis Group, London, pp 2–15

Crosta GB, Agliardi F (2003) Failure forecast for large rock slides by surface displacement measurements. Can Geotech J 40:176–191. doi:10.1139/t02-085

Di Crescenzo G, Santo A (2007) High-resolution mapping of rock fall instability through the integration of photogrammetric, geomorphological and engineering-geological surveys. Quat Int 171–172:118–130. doi:10.1016/j.quaint.2007.03.025

Farina P, Leoni L, Babboni F, Coppi F, Mayer L, Ricci P (2011) IBIS-M, an innovative radar for monitoring slopes in open-pit mines. In: proceedings of International Symposium on Rock Slope Stability in Open Pit Mining and Civil Engineering

Ferretti A, Prati C, Rocca F (2001) Permanent scatterers in SAR interferometry. IEEE Trans Geosci Remote Sens 39:8–20

Franceschetti G, Migliaccio M, Riccio D, Schirinzi G (1992) SARAS: a synthetic aperture radar (SAR) raw signal simulator. IEEE Trans Geosci Remote Sens 30:110–122

Frukacz M, Presl R, Wieser A, Favot D (2016) Pushing the Sensitivity Limits of TPS-based Continuous Deformation Monitoring of an Alpine Valley. In: Proceedings of JISDM 2016 Vienna

Gigli G, Morelli S, Fornera S, Casagli N (2014) Terrestrial laser scanner and geomechanical surveys for the rapid evaluation of rock fall susceptibility scenarios. Landslides 11:1–14. doi:10.1007/s10346-012-0374-0

Gupta M, Wong E (2007) Microwaves and metals. Wiley, Singapore

Hanssen R (2002) Radar interferometry. Data interpretation and error analysis. Kluwer Academic Publishers

Huang CJ, Chu CR, Tien TM, Yin HY, Chen PS (2012) Calibration and deployment of a fiber-optic sensing system for monitoring debris flows. Sensors (Switzerland) 12:5835–5849. doi:10.3390/s120505835

Intrieri E, Traglia FD, Ventisette CD, Gigli G, Mugnai F, Luzi G, Casagli N (2013) Flank instability of Stromboli volcano (Aeolian Islands, southern Italy): integration of GB-InSAR and geomorphological observations. Geomorphology 201:60–69. doi:10.1016/j.geomorph.2013.06.007

Kampes BM (2006) Radar interferometry. Persistent scatterer technique. Springer, Netherlands

Knott E, Shaeffer J, Tuley M (2004) Radar cross section. SciTech Publishing, Raleigh

Loew S, Gitschig V, Moore JR, Keller-Signer A (2012) Monitoring of potentially catastrophic rockslides. In: Eberhardt E, Froese C, Turner K, Leroueil S (eds) Landslides and engineered slopes: protecting society through improved understanding. Taylor & Francis Group, London, pp 101–116

Luzi G, Pieraccini M, Mecatti D, Noferini L, Guidi G, Moia F, Atzeni C (2004) Ground-based radar interferometry for landslides monitoring: atmospheric and instrumental decorrelation sources on experimental data. IEEE Trans Geosci Remote Sens 42:2454–2466. doi:10.1109/TGRS.2004.836792

Luzi G, Noferini L, Mecatti D, Macaluso G, Pierracini M, Atzeni C (2009) Using a ground-based SAR interferometer and a terrestrial laser scanner to monitor a snow-covered slope: results from an experimental data collection in Tyrol (Austria). IEEE Trans Geosci Remote Sens 47:382–393. doi:10.1109/TGRS.2008.2009994

Mazzanti P (2011) Displacement monitoring by terrestrial SAR interferometry for geotechnical purposes. Geotech News 29:25–28

Mazzanti P, Bozzano F, Cipriani I, Prestininzi A (2014) New insights into the temporal prediction of landslides by a terrestrial SAR interferometry monitoring case study. Landslides. doi:10.1007/s10346-014-0469-x

Miller PK, Vessely M, Olson LD, Tinkey Y (2013) Slope stability and rock-fall monitoring with a remote interferometric radar system. Geotech Spec Publ 304–318

Monserrat OH, Crosetto M, Luzi G (2014) A review of ground-based SAR interferometry for deformation measurement. ISPRS J Photogramm Remote Sens 93:40–48. doi:10.1016/j.isprsjprs.2014.04.001

Noferini L, Pieraccini M, Mecatti D, Luzi G, Atzeni C, Tamburini A, Broccolato M (2005) Permanent scatterers analysis for atmospheric correction in ground-based SAR interferometry. IEEE Trans Geosci Remote Sens 43:1459–1470. doi:10.1109/TGRS.2005.848707

Rabatel A, Deline P, Jaillet S, Ravanel L (2008) Rock falls in high-alpine rock walls quantified by terrestrial lidar measurements: a case study in the Mont Blanc area. Geophys Res Lett. doi:10.1029/2008GL033424

Rödelsperger S (2011) Real-time processing of ground based synthetic aperture radar (GB-SAR) measurements. Dissertation, Technische Universität Darmstadt

Rüeger J (2002) Refractive index formulae for radio waves. In: Fig. XXII International Congress, Washington, pp 1–13

Severin J, Eberhardt E, Leoni L, Fortin S (2011) (2011) Use of ground-based synthetic aperture radar to investigate complex 3-D pit slope kinematics. Proceedings of Slope Stability, In

Seymour MS, Cumming IG (1994) Maximum likelihood estimation for SAR interferometry. Proc IGARSS '94–1994 I.E. Int Geosci Remote Sens Symp 4:2272–2275. doi:10.1109/IGARSS.1994.399711

Skolnik MI (1990) Radar Handbook. McGraw-Hill, Boston

Ulaby FT, Bengal TH, Dobson MC, East JR, Garvin JB, Evans D (1990) Microwave dielectric properties of dry rocks. IEEE Trans Geosci Remote Sens 28:325–336

Volkwein A, Schellenberg K, Labiouse V, Agliardi F, Berger F, Bourrier F, Dorren LKA, Gerber W, Jaboyedoff M (2011) Rockfall characterisation and structural protection—a review. Nat Hazards Earth Syst Sci 11:2617–2651. doi:10.5194/nhess-11-2617-2011

Wyllie DC, Mah CW (2004) Rock slope engineering. Spon Press, London

M. Frukacz (✉) · **A. Wieser**

Institute of Geodesy and Photogrammetry (IGP), ETH Zürich,
Stefano-Franscini-Platz 5, 8093, Zürich, Switzerland
e-mail: mariusz.frukacz@geod.baug.ethz.ch